Journal of Alloys and Compounds 999 (2024) 175104

Contents lists available at ScienceDirect

Journal of Alloys and Compounds

journal homepage: www.elsevier.com/locate/jalcom

Unraveling dynamic Jahn-Teller effect and magnetism in $FeTiF_6 \times 6H_2O$ single crystal

Mikhail S. Platunov [a,*], Natalja A. Fedorova [b], Yulia V. Pyastolova [b], Natalja M. Laptash [c], Yuriy V. Knyazev [b], Felix N. Tomilin [b], Andrey A. Dubrovskiy [b,*]

[a] Synchrotron Radiation Facility SKIF, Boreskov Institute of Catalysis SB RAS, Kol'tsovo 630559 , Russia
[b] Kirensky Institute of Physics, Federal Research Center KSC SB RAS, Krasnoyarsk 660036, Russia
[c] Institute of Chemistry, Far Eastern Branch of RAS, Vladivostok 690022, Russia

ARTICLE INFO

Keywords:
Dynamic Jahn-Teller effect
Density functional theory
B3LYP
Magnetic and electronic properties
Mössbauer spectroscopy
XMCD
XANES

ABSTRACT

Hydrated iron fluoridotitanate ($FeTiF_6 \times 6\ H_2O$) single crystals are fascinating magnetic materials with unique properties. To understand the underlying mechanisms, this study combines X-ray absorption near-edge structure (XANES) and X-ray magnetic circular dichroism (XMCD) techniques, complemented by density functional theory (DFT) calculations. Polarization-dependent X-ray absorption spectroscopy, encompassing XANES and XMCD, is a powerful technique for probing the local structures and magnetic properties of materials. It is element-selective, bulk-sensitive, and compatible with a wide range of experimental conditions. In this study, we used XANES and XMCD spectroscopies to investigate the local structures and magnetic properties of Fe and Ti in $FeTiF_6 \times 6\ H_2O$ single crystals. XANES analysis revealed distinct local environments around Fe and Ti, providing insights into their coordination environments. Element-selective magnetization measurement at the Fe *K*-edge demonstrated that iron sites in the oxidation state Fe^{2+} have an unambiguous paramagnetic contribution to the magnetization along the *b*-axis. Notably, the absence of an XMCD signal at the Ti *K*-edge confirmed the absence of a magnetic moment in Ti atoms within the crystal. DFT calculations corroborate the experimental findings and provide insights into the electronic structure and magnetic interactions. The combined results provide a comprehensive understanding of the dynamic Jahn-Teller effect in $FeTiF_6 \times 6\ H_2O$ single crystals, highlighting the significance of polarization-dependent X-ray absorption spectroscopy in unraveling the intricate magnetic behavior of such materials. This study contributes to the fundamental understanding of magnetism in these materials and paves the way for the development of novel magnetic materials with tailored properties.

1. Introduction

Numerous studies related to the application of fluoride have primarily focused on the conventional and physical chemistry of inorganic fluorides. However, fundamental studies are crucial for developing multifunctional fluoride materials with applications in energy conversion processes [1,2], electronics [3], optoelectronics [4], and spintronics [5]. The $FeTiF_6 \times 6\ H_2O$ (hydrated iron fluoridotitanate) material belongs to the extensive family of $ABF_6 \times 6\ H_2O$ compounds (where A = Mg, Zn, Fe, Co, Ni, Mn, or Cd and B = Ti, Si, Ge, Sn, or Zr). These compounds crystallize in the rhombohedrally distorted CsCl structure [6] and exhibit unique properties such as frustrated magnetism [7–14] and rare-earth-free red-emitting phosphorescence [15]. Despite their undoubted fundamental importance, these materials remain understudied.

Transition metal fluoride hexahydrates are classified as vibronic crystals due to the alternating $[A(H_2O)_6]^{2+}$ and $[BF_6]_2$ octahedra, which are bound by O – H ••• F hydrogen bonds [16,17]. These results in the emergence of vibronic states, which are coupled vibrations of nuclei and electrons. In these crystals, the system is delocalized over all energy minima, and tunneling between single low-symmetry states occurs [18]. Consequently, the molecules retain their individuality in both the ground and excited states, are weakly perturbed by the intracrystalline field, and have weakly overlapping wave functions. The excited state of a molecule is not localized and can move from molecule to molecule.

Typically, these materials undergo a phase transition near room temperature from a trigonal $R3^{-}$ to a monoclinic phase P21/c phase. The temperature of this transition can also depend on the type of

* Corresponding authors.
E-mail addresses: m.s.platunov@srf-skif.ru (M.S. Platunov), andre-do@yandex.ru (A.A. Dubrovskiy).

https://doi.org/10.1016/j.jallcom.2024.175104
Received 27 March 2024; Received in revised form 7 May 2024; Accepted 5 June 2024
Available online 6 June 2024

hydrogen isotope in the crystal structure [19]. This phase transition can be tuned at relatively low pressure, making this family of materials of great interest for studying phase transitions and investigating critical phenomena [20]. In the case of the crystal under investigation, a recent X-ray diffraction analysis of $FeTiF_6 \times 6\ H_2O$ single crystals revealed that the crystal structure belongs to space group $R3^-$ at room temperature and transforms to space group P21/c upon cooling [6]. However, more recent work [9] initially presented contradictory results, with static magnetic measurements seemingly contradicting those obtained by Mössbauer spectroscopy. The authors of [7,8,10–13] did not have the opportunity to analyze these results in detail. In addition to the magnetic ordering mechanism proposed by the authors of [9], electron paramagnetic resonance measurements suggest that the strong anisotropy of the crystal and possible exchange interactions through hydrogen bonds [21,22] could explain the emergence of long-range magnetic order below $T_N = 8$ K observed in magnetic measurements [23]. Another possible explanation for the discrepancy between magnetic and Mössbauer measurements is the presence of magnetic Ti^{3+} ions. This hypothesis could be verified through XANES/XMCD spectroscopy and density functional theory (DFT) calculations. A crystal containing a hydrated iron ion and a titanium fluoride ion may exhibit Jahn-Teller distortions due to unique chemical structure characteristics and general considerations. In a magnetic system containing an ion with orbital degeneracy (known as a Jahn-Teller ion), we can expect the following: (1) the crystal structure will distort, resulting in decreased symmetry; (2) structural phase transitions will occur; (3) the magnetic structure may become complex; (4) anomalously strong magnetic anisotropy may be observed. Given that the central iron ion has weak coordination bonds with six water molecules, we expect that in the normal state, the magnetic moments of iron will not be linked in any way, leading to a paramagnetic case. Experimental absorption spectra of transition metal ions cannot be used as evidence for the distortion of the ion environment because the spectral bands are too broad. Additionally, the IR and Raman spectra of these ions lack characteristic split lines. In the case of iron ions, optical spectra provide only tentative evidence for the influence of level degeneracy. However, alternative explanations for the same results are often possible and require more careful study. For iron ions with d^6 configurations, where transitions occur between doubly and triply degenerate levels, the spectral lines should be broader than for other ions. The Jahn-Teller effect is also of interest in many other areas of theoretical research.

From a quantum chemical perspective, it is essential to consider the diverse bonding interactions present in these crystals. These interactions include ionic bonds in TiF_6, complex bonds formed through a donor-acceptor mechanism in hydrated iron $Fe(H_2O)_6$, and hydrogen bonds between the hydrate shell of the iron ion and fluorine ions. Accurately describing the intricate electronic structure of such crystals necessitates the application of sophisticated computational methods, such as hybrid or *meta*-GGA functionals in conjunction with appropriate basis sets.

In this study, we investigate the element-selective magnetic properties of the $FeTiF_6 \times 6\ H_2O$ single crystal using XANES/XMCD spectra. These spectra provide valuable insights into the local coordinate geometry, ligand type, oxidation state, electronic configuration, and magnetic state of Fe and Ti ions. By combining computational methods with experimental procedures, we aim to obtain a comprehensive understanding of the key parameters of the crystals under investigation, as well as the distribution of electric charge within these systems. This combined approach allows us to elucidate the fundamental mechanisms underlying the magnetic properties and electronic structure of $FeTiF_6 \times 6\ H_2O$. Our findings shed light on the complex interplay between different types of bonds and their influence on the overall behavior of the material.

2. Experimental details

2.1. X-ray absorption near edge structure (XANES) and X-ray magnetic circular dichroism (XMCD)

X-ray absorption spectroscopy (XAS) was performed in collaboration with the ID12 beamline at the European Synchrotron Radiation Facility (ESRF). The Fe *K*-edge and Ti *K*-edge XANES and XMCD spectra were recorded using circularly polarized X-rays generated by the first (for Ti *K*-edge) and second (for Fe *K*-edge) harmonics of the HELIOS-II type helical undulator (HU-52). A fixed-exit double-crystal monochromator equipped with a pair of Si (111) crystals was employed to monochromatize the X-ray beam. The photon energy of the double-crystal monochromator was calibrated at the Ti *K*-edge threshold of a titanium foil at 4966.4 eV. Samples were mounted on a cold finger of an "amagnetic" He flow cryostat. The cold finger was inserted into a cold bore of a superconducting solenoid capable of generating a maximum magnetic field of 17 Tesla. The total fluorescence yield signal was collected by a Si photodiode [24] mounted in a back-scattering geometry. This detection method was preferred over total electron yield due to its insensitivity to magnetic fields and its ability to probe the bulk properties of the sample. Spectra were measured with the crystal's third-order crystallographic axis perpendicular to both the X-ray wave vector and the applied magnetic field, aligning the **b**-axis parallel to both. This precise orientation is crucial for XMCD measurements, as the technique's effectiveness hinges on the alignment between the magnetic field, the X-ray wave vector, and the crystal's magnetization axis. To ensure the accuracy of the results, each measurement was repeated 24–28 times, and the average value of the spectrum was taken into account. The XMCD signal was obtained by subtracting XANES spectra measured with opposite helicities of the incoming photons at a fixed magnetic field. Measurements were performed for two directions of applied magnetic field, parallel and antiparallel to the incoming X-ray wave vector, to ensure the correctness of the final XMCD signals. The element-selective magnetization curve at the Fe *K*-edge was recorded by monitoring the intensity of the XMCD signal at 7115.8 eV as a function of the applied magnetic field (±17 T). All data processing included corrections for self-absorption effects, calibration of the energy scale, removal of the pre-edge background by straight-line fitting, and removal of the post-edge background by second-order polynomial fitting. The XANES spectra were also normalized to 1, and this normalization was applied to all spectra in the paper. All XMCD spectra are given after polarization rate correction.

2.2. Mössbauer spectroscopy and magnetization measurements

The magnetization was measured with a vibrating sample magnetometer (VSM) and a Quantum Design PPMS 9 T Physical Property Measurement System. The sample parameters are: mass is about ~30 mg, length is ~5.5 mm and width is ~3.5 mm. The crystal placed in a cylindrical chamber in such a way that the sample was tightly clamped and could not turn in a magnetic field. To check the correctness of the measurements, the same sample was examined on a device Quantum Design PPMS 9 T Physical Property Measurement System with the standard VSM supplied with this instrument. It should be noted that the magnetization curves obtained with two different devices were found to be fully identical.

The Mössbauer spectra of the grinded single crystal were recorded on MS-1104Em spectrometer in the transmission geometry with a Co^{57} (Rh) radioactive source in the temperature range of 4.2–300 K using a CFSG-311-MESS cryostat with a sample in the exchange gas based on a closed-cycle Gifford-McMahon cryocooler (Cryotrade Engineering). The spectra were processed by varying the entire set of hyperfine parameters using the linear least-squares method.

2.3. Computational details and analysis of crystal structure

The atomic and electronic structure and spin states of various regular 3D crystal lattices of $FeTiF_6 \times 6\ H_2O$ were investigated in reciprocal space using *ab initio* DFT approach. Two hybrid exchange-correlation functionals, PBE0–13 [25] and B3LYP [26], were employed in conjunction with the pob-TZVP-rev2 basis set [27]. Hybrid or meta-GGA methods are more suitable for analyzing possible magnetic states in complex crystals with ionic, covalent, and hydrogen bonds, as simple GGA methods often fail to accurately such systems. Both PBE0–13 and B3LYP functionals yielded similar results, with PBE0–13 providing values closer to experimental magnetic moment values. All PBE0–13/*pob*-TZVP-*rev2* and B3LYP/*pob*-TZVP-*rev2* electronic structure calculations of $FeTiF_6 \times 6\ H_2O$ were performed using CRYSTAL 17 software package [28].

DFT modeling of the crystal structure also allows for the calculation of Mössbauer parameters using the Crystal package. By comparing these calculated parameters with experimental data from Mössbauer spectroscopy, the accuracy of the obtained results at the level of electron-nuclear interactions can be verified. According to the calculation results, the values of the chemical shift and the quadrupole splitting at 300 K obtained using the B3LYP approximation are 0.97 mm/s and 2.49 mm/s, respectively, after taking into account the calibration factor [29]. The relative error compared to the experimental results is approximately 24 % for both superfine parameters, indicating a good optimization of the crystal structure.

The experimental atomic structure at the low temperature (LT-crystal) 233 K [6] was used to calculate the electronic properties. The $FeTiF_6 \times 6\ H_2O$ has a P 21/c (monoclinic, space group number 14) unit cell with parameters $a = 6.6624$, b = 9.7082, c = 8.5901, α, β = 90.0, γ = 100.6 (Fig. 1, a, b).

To simulate the ferromagnetic properties, spin-polarized electronic structure calculations were performed for unit cells in P1 symmetry consisting of 52 atoms (two Fe ions, two Ti ions, etc. Fig. 1, a) for the crystal at 233 K, and for both crystal configurations at 293 K, the cell in P1 symmetry contained 78 atoms (three Fe ions, three Ti ions, etc. Fig. 1, c1) with magnetic moments localized on *d*-elements (Table 1). For a possible optical transition, the calculations showed an indirect energy band gap E = 3.80 eV, corresponding to 327 nm in the LT-crystal at 233 K. An indirect energy band gap E = 5.06 eV, corresponding to 246 nm for a possible optical transition, was obtained for both configurations of RT-crystals. From the values of the magnetic moments (Table 1), we can conclude that iron in this structure corresponds to oxidation state +2 and titanium to +4.

After structure optimization, the LT-crystal structure exhibited an increase in parameter ***a*** by 0.050 Å (from 6.662 Å to 6.712 Å), a decrease in parameter ***b*** by 0.084 Å (from 9.708 Å to 9.624 Å), and a decrease in parameter ***c*** by 0.157 Å (from 8.590 Å to 8.433 Å). Conversely, the RT-C1 crystal structure showed a decrease in parameter ***a*** by 0.101 Å (from 9.813 Å to 9.712 Å), a decrease in parameter **b** by 0.101 Å (from 9.813 Å to 9.712 Å), and an increase in parameter **c** by 0.068 Å (from 9.865 Å to 9.933 Å). Finally, the RT-C2 crystal structure exhibited a decrease in parameter **a** by 0.147 Å (from 9.813 Å to 9.666 Å), a decrease in parameter **b** by 0.147 Å (from 9.813 Å to 9.666 Å), and an increase in parameter **c** by 0.083 Å (from 9.865 Å to 9.948 Å).

In the case of Fe^{2+} for the LT-crystal, large distortions are not expected due to orbital and spin degeneracy. For the Fe^{2+} ion with d^6 configuration in the octahedral field of weak ligands, triple degenerate t_{2g} and double degenerate e_g charge distributions are expected. Therefore, for a given octahedral field of d^6 ligands, small distortions of the octahedron surrounding the iron ion are anticipated. This fact can be observed in the experimental crystal structure (Fig. S1). The octahedron consisting of water molecules ($Fe(H_2O)_6$) is slightly stretched along the z-axis (Fe1-O1 = 2.10 Å, Fe1-O2 = 2.11 Å, Fe1-O3 = 2.10 Å, Fig. S1), while the TiF_6 octahedron is almost free of distortion (Ti1-F1 = 1.86 Å, Ti1-F2 = 1.86 Å, Ti1-F3 = 1.86 Å; changes are only noticeable in thousandths of an angstrom, Fig. S1). This small tetragonal stretching is not expected to significantly affect the additional splitting of the t_{2g} plane. The interaction of the magnetic moments of iron ions with four unpaired electrons has a quantum mechanical nature, which depends on the distance between the magnetic ions as well as on their mutual geometrical arrangement. For the LT-crystal, the distance between Fe1 - Fe1 along the **a**-axis is 6.66 Å, along the **b**-axis is 9.71 Å, and along the **c**-axis is 8.59 Å (Fig. 1, a). The distance between Fe1 - Fe2 is 6.48 Å and Fe2 - Fe2 is 6.66 Å (Fig. 1, a).

The phase transition for this crystal is observed at 273 K. At room temperature (RT-crystal), the crystal is trigonal (Figs. 1, c1-f2) with symmetry R −3 (trigonal) and lattice parameters $a = 9.8127$ Å, b = 9.8127 Å, c = 9.8650 Å, α, β = 90.0°, γ = 120.0° (Fig. 1, c1-c2). When comparing the different phases, large changes in lattice parameters can be observed: **a** – from 9.8127 Å to 6.6624 Å (47 % change), **b** – from 9.8127 Å to 9.7082 Å (1 % change); **c** – from 9.8650 Å to 8.5901 Å (15 % change); **γ** – from 120.0° to 100.6° (19 % change) (RT-crystal is taken as 100 %). Two different octahedral orientations for iron and titanium ions with the same (50/50) fraction are observed for this crystal (Fig. 1, c1-f2). Fig. 1 (c1-f2) shows different views of the RT-crystal: c1-c1 – top view of the two orientations of hydrate and hexafluoride octahedrons; d1-d2 – combined orientations, top and side views; e1-e2 – hydrate octahedrons of iron ions; f1-f2 – hexafluoride octahedrons of titanium ions. The octahedra themselves are undistorted for the hydrate shell (Fe1-O1 bond length = 2.11 Å, Fig. S2, b), and the hexafluoride octahedra of titanium (Ti1 – F'1 = 1.8579 Å, Ti1 – F''2 = 1.8582 Å, Fig. S2, c) are almost undistorted. This feature of the crystal at room temperature can be explained by the dynamical Jahn-Teller effect. The absence of characteristic splitting lines in the vibrational and Raman spectra of these ions can be attributed to the unchanged modes of the octahedral vibrations (Figs. 1, e1, e2, f1, f2) and lack of observation of modes related to the orientation of the octahedrons relative to the directions in the crystal in this type of spectroscopy.

2.4. Mössbauer spectroscopy

Since the Mössbauer measurements of the sample performed earlier [9] do not show any Zeeman splitting in the temperature range of 4–300 K, we can analyze the pure response of the local environment under the action in the region of magnetic (according to magnetometry data) and structural transitions. For this purpose, we used the temperature dependence of the linewidth difference and the quadrupole splitting of the Mössbauer spectra (Fig. 2(a) and (b)). Above the structural transition temperature, the octahedral environment of iron has nearly cubic symmetry. Quantitative estimation from experimental X-ray diffraction data can be obtained by calculating the value of the principal component of the electric field gradient tensor according to the expression:

$$V_{zz} = \sum 2e\frac{3\cos^2\theta - 1}{r^3} \quad ,$$

Here, $\mathbf{V_{zz}}$ is the electric field gradient in the direction of the main axis of the oxygen octahedron. **θ** is the angle between this axis and the direction of the neighboring oxygen ion, **e** is the electron charge, and **r** is the metal-oxygen distance.

Following this equation, the value of V_{zz} is calculated to be 1.3e17 V/m^2 above the structural transition temperature. Below the structural transition, the local distortions drastically increase and the V_{zz} value becomes higher by two orders (V_{zz} = 2.1e19 V/m2). This suggests that the observed quadrupole splitting is only due to the action of the extra d^6 electron on the lower t_{2g} level. However, although we see an increase in the degree of the electric field gradient on the iron nuclei, the value of V_{zz} remains small. For comparison, the values obtained are four orders of magnitude smaller than those in known iron compounds [30]. Taking these data into account, it is possible to estimate the lattice contribution

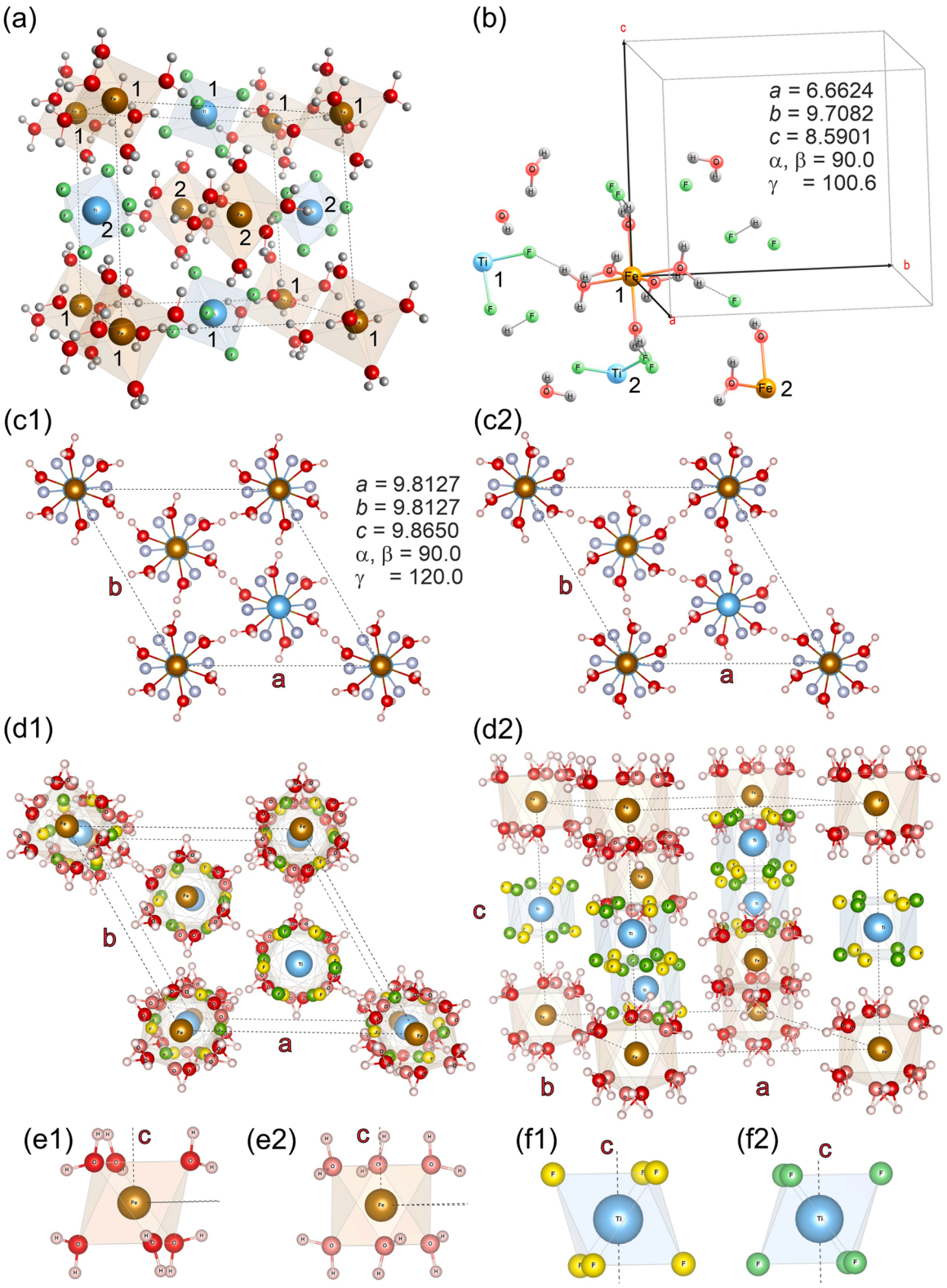

Fig. 1. Experimental atomic structure of $Fe(H_2O)_6 \times TiF_6$ at different temperatures (233 K – low temperature (LT-crystal); 293 K – room temperature (RT-crystal) [6]). (a) Crystal structure of LT crystal at 233 K (crystal structure P21/c, monoclinic, space group number 14). (b) Primitive cell for theoretical calculations, 52 atoms. (c1)-(f2) Atomic structure of RT crystal at 293 K (crystal structure R −3, trigonal, space group number 148). (c1) Top view of the atomic structure of the RT crystal at 293 K in configuration c1. (c2) Top view of the atomic structure of the RT crystal at 293 K in configuration c2. (d1) Top and side views of the atomic structure of the RT crystal at 293 K in configuration c1. (d2) Top and side views of the atomic structure of the RT crystal at 293 K in configuration c2. (e1) Hydrated octahedron of iron ion $[A(H_2O)_6]^{2+}$ of configuration c1. (e2) Hydrated octahedron of iron ion $[A(H_2O)_6]^{2+}$ of configuration c2. (f1) Hexafluoride octahedron of titanium ion $[BF_6]_2$ of configuration c1. (f2) Hexafluoride octahedron of titanium ion $[BF_6]_2$ of configuration c2. Color coding: brown for Fe atoms, blue for Ti atoms, light red for H, yellow for F in configuration c1, green for F in configuration c2, and red for O atoms.

Table 1
Values of partial electronic charges (e^-) and magnetic moments (μ_B) on iron and titanium ions in ferromagnetic state.

Structure	[a]Metal ion	DFT hybrid functionals			
		PBE0-13		B3LYP	
		Charge	Magnetic moment**	Charge	Magnetic moment**
LT	Fe_1	1.151	3.866	1.039	3.814
	Fe_2	1.152	3.866	1.039	3.814
	Ti_1	1.859	0.001	1.758	0.001
	Ti_2	1.860	0.001	1.758	0.001
RT_C1	Fe_1	1.145	3.887	1.104	3.821
	Fe_2	1.145	3.887	1.104	3.821
	Fe_3	1.145	3.887	1.104	3.821
	Ti_1	1.815	0.000	1.781	0.001
	Ti_2	1.815	0.000	1.781	0.001
	Ti_3	1.815	0.000	1.781	0.001
RT_C2	Fe_1	1.144	3.887	1.108	3.822
	Fe_2	1.144	3.887	1.108	3.822
	Fe_3	1.144	3.887	1.108	3.822
	Ti_1	1.813	0.000	1.781	0.001
	Ti_2	1.813	0.000	1.781	0.001
	Ti_3	1.813	0.000	1.781	0.001

[a] According to the Fig. 1.

to the value of the quadrupole splitting. The lattice contribution to the value of the quadrupole splitting in the paramagnetic state can be defined in terms of the Sternheimer anti-shielding effect [31,32] as follows

$$QS = (1-\gamma_\infty)\frac{1}{2}eQV_{zz}\left(1+\frac{\eta^2}{3}\right)^{1/2}$$

In this expression, γ_∞=-11.51 is the Sternheimer anti-shielding factor for the Fe^{2+} cation [33], and $\eta = (V_{xx}-V_{yy})/V_{zz}$ is the asymmetry parameter describing the deviation from axial symmetry.

In our case, the change in local distortions during the substitution is reflected in the value of the parameter V_{zz}, which is calculated from the X-ray structure data. For the sample, the calculated value of the quadrupole splitting (QS) is 0.018 mm/s, while the experimental value is 3.28 mm/s at 300 K. This indicates that the formation of QS in the sample is primarily due to the valence contribution across the entire temperature range. The growth of the QS with decreasing temperature (Fig. 2c) can be attributed to the influence of the d^6 electron. This enables the Kronig-Van Fleck mechanism, where the electron's orbital motion is modulated by crystal lattice vibrations. The strong spin-orbit interaction then influences the electron spin and consequently the magnetic behavior of the sample. The sample undergoes a structural transition driven by the dynamical Jahn-Teller effect. The effect reduces the local symmetry, increasing the QS value in the Mössbauer spectrum, while the spin-orbit coupling attempts to maintain the degeneracy. At low temperatures (Fig. 2a), we observe a decrease in the difference in the width of the Mössbauer lines, suggesting that the competition between the spin-orbit interaction and the Jahn-Teller effect shifts in favor of the spin-orbit interaction at low temperatures.

Using the Crystal package, we performed DFT calculations of the optimized $FeTiF_6 \times 6\,H_2O$ crystal structure above and below the structural transition to obtain the theoretical QS value. These values are represented by stars in Fig. 2. Comparison of the experimental Mössbauer data and the theoretical values reveals that the calculated values are close to the experimental ones, with a calculation error of 24 %. The trend of the theoretical QS change is also consistent with the observable data. Thus, our DFT calculations provide a reliable model for analyzing experimental data. In contrast, the calculated value of the QS of the Ti^{4+} nuclei in the structure is approximately 0.3 mm/s, which is relatively small and can be attributed to the pure lattice impact due to the fully unoccupied 3*d*-shell of Ti^{4+}. Therefore, we propose that the observed distortion is primarily caused by the Jahn-Teller effect of iron

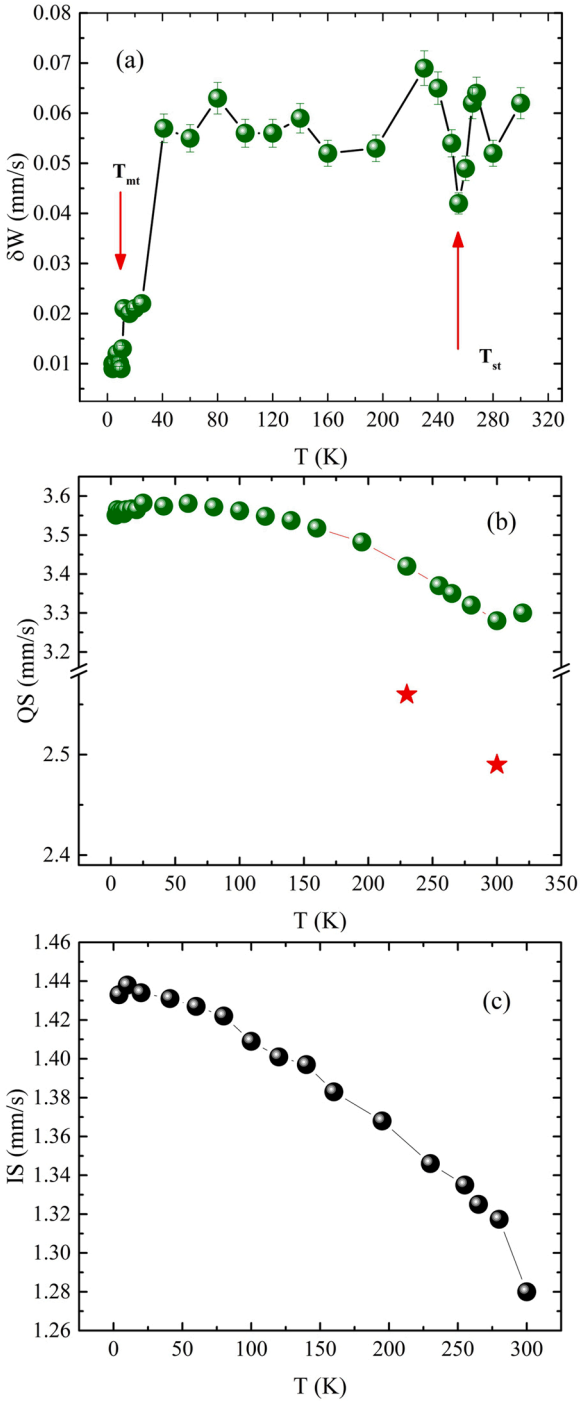

Fig. 2. Mössbauer spectroscopy data. (a) Temperature dependence of the linewidth difference (δW) in the quadrupole doublet, as measured by Mössbauer spectroscopy. The linewidth difference provides a measure of the inhomogeneity in the sample. Corresponding temperatures of structural (T_{st}) and magnetic (T_{mt}) transition are shown. (b) Temperature dependence of the quadrupole splitting (QS) with the calculated data by DFT (red stars). (c) Temperature dependence of the chemical shift (IS).

2+ cations.

3. Results and discussion

We employed X-ray Absorption Near-Edge Structure (XANES) and X-ray magnetic circular dichroism (XMCD) techniques to investigate the spatial arrangement, coordination number, and magnetic properties of

Ti and Fe atoms. These techniques provide valuable insights into the electronic and magnetic properties of materials. XANES offers information about the spatial arrangement and coordination number of Ti and Fe atoms by probing the unoccupied electronic states near the absorption edges. On the other hand, XMCD, a derivative technique of XANES, is sensitive to the magnetic properties of the sample. It allows us to probe the magnetic moments and exchange interactions between the Ti and Fe ions. At the transition metal $L_{3,2}$-edges, XMCD directly probes the magnetic 3*d* orbitals, providing quantitative information about the spin and orbital momenta. However, this technique is primarily applicable to thin films and nanoparticles due to the ultra-high vacuum requirement and limited penetration depth of the incident X-rays. In contrast, transition metal *K*-edge XMCD operates in the hard X-ray regime and probes the delocalized 4*p* orbitals. While it does not directly provide magnetic information, it offers the possibility to obtain fine structural information. We propose to interpret our results based on the 3*d*-4*p* orbital overlap and the local symmetry of the Fe and Ti ions. Furthermore, we can explain the exchange interaction between the photoelectron in the delocalized 4*p* states and the unpaired electrons in the 3*d* orbitals. This interaction consists of the direct exchange interaction and orbitals mixing, which depends on the local symmetry of the transition metal.

The use of *K*-edge XMCD is particularly advantageous for obtaining local magnetic information, confirming macroscopic measurements, and studying states inaccessible by other techniques. In the case of the $FeTiF_6 \times 6\ H_2O$ single crystal, the relative sign of the *K*-edge XMCD signal can provide a clear indication of the nature of the exchange interaction between the Fe and Ti ions. Additionally, it allows us to identify the metallic ion carrying the larger magnetic moment. To gain a deeper understanding of the magnetism mechanism, we performed XMCD measurements at the Fe and Ti *K*-edges at room temperature and 2.5 K (well below the magnetic transition temperature) on hydrated iron fluoridotitanate single crystals.

3.1. X-ray absorption spectroscopy analysis at Fe K-edge

The XANES and XMCD spectra measured at the Fe-*K* absorption edge for our single crystal sample are presented in Figures S3 and S4. Fig. S3 (a) shows the corresponding XANES spectrum. Three distinct regions can be observed near the Fe-*K* XANES and XMCD spectra, which are most clearly seen in Figure S4. The first region **(1)** corresponds to the 1*s*-3*d* quadrupole transition, indicating possible Fe(3*d*, 4*p*) hybridization and allowing electric dipole transitions toward the pre-edge. Such transitions are strictly forbidden in centrosymmetric sites. A negative XMCD peak at the pre-edge is observed with a width of approximately 4 eV and an amplitude of 1.5×10^{-3} compared to the edge jump of unity. The next region (**2**) represents the 1*s*-4*p* electric dipole transition, where a large positive XMCD peak is observed at 7129 eV (Figure S4). The last region of interest **(3)** arises from the so-called multielectron excitation, where part of the energy of the high-energy photon is absorbed by a 1 *s* electron (1*s*-4*p*), and the excess energy of this photon is sufficient to excite a 3*p* electron (3*p*-3*d*). The XMCD spectrum in the pre-edge region (7110 – 7120 eV, Fig. S3(b)) consists of two negative peaks, a small one at 7114.5 eV and a large one at 7115.8 eV. The integral over this measured energy range is negative, indicating that the Fe 3*d* state has a magnetic moment parallel to the magnetic field. Unfortunately, the spin magnetic moment cannot be derived from hard X-rays. Nevertheless, the obtained results are consistent with macroscopic observations of the magnetization behavior. Moreover, the measured shape of XMCD is primarily identical to that of the Fe^{2+} octahedral site, for which the absence of an inversion center in the crystallographic site allows for 3*d*-4*p* hybridization. As seen in Fig. S3(c) and S5, the Fe-*K* XMCD signal was measured as a function of the applied magnetic field under the following condition: photon energy 7115.8 eV for Fe and magnetic field ranging from −17 T to 17 T. It can be observed that the microscopic magnetization of Fe follows the macroscopic magnetization and exhibits paramagnetic behavior.

It is known that the energy position and shape of the Fe pre-edge and edge features could be influenced by both coordinate geometry and oxidation state [34,35]. Fig. 3(a) shows the measured pre-edge features on the Fe *K*-edge side. The Fe pre-edge peak feature is considered to be Fe occupied in octahedral coordination with a relative oxidation state close to 2+ [35–38]. The first peak feature at around 7113.81 eV corresponds to both Fe_0 3*d* and Fe 3*d* mixed with 4*p* character and could be attributed to the 1 *s* hybridized Fe_0 3*d*-4*p* and some delocalized Fe 3*d*-4*p* with O 2*p* character.

3.2. X-ray absorption spectroscopy analysis at Ti K-edge

Pre-edge and main-edge features of the XANES *K*-edge spectra are determined by electronic transitions between bound states [39]. For instance, the pre-edge peak in the Ti *K*-edge XANES spectra is attributed to the transition from the 1 *s* energy levels to bound 3*d* molecular orbitals [40–42]. Shifts in energy observed in the XANES spectra are influenced by the oxidation state and coordination chemistry, with higher energies corresponding to higher oxidation state. In Figure S6(c), the titanium *K*-edge XANES spectra exhibit a distinct and consistent shift towards higher energies for the absorption edge features obtained from standard reference material with exclusively metallic Ti to ionic Ti^{4+}. Numerous studies have demonstrated that the pre-edge also serves as an indicator of changes in the valence state [43]. Furthermore, the peak of the Ti *K*-edge XANES spectra associated with the 1*s*-3*d* transition can be utilized to determine the Ti valence.

Figure S6(a,b) reveals that the Ti *K*-edge XANES spectra also exhibit peaks just below the main X-ray absorption edge in the pre-edge energy region. Notably, the XANES region of the Ti *K*-edge absorption spectrum is rich in structure, which is sensitive to the details of the Ti coordination environment and its valence state. Previous studies have observed that the near-edge X-ray absorption spectra of Ti^{4+} can exhibit up to nine resolvable absorption features, which can be categorized into three subgroups for further analysis. The energy range of interest in this study is between 4960 and 5020 eV. Beyond 5020 eV, the observed features have significantly reduced amplitude and are generally attributed to single scattering EXAFS. The first two features appear in the pre-edge region, where transitions to unfilled molecular orbital levels are observed. These are best illustrated in the spectrum of the sample shown in Fig. S6(b). The separation between the first and second features is approximately 2.1 eV in the spectrum, and these features can be fitted by two Gaussian functions (Fig. 3b).

The energies of the pre-edge features are relatively insensitive to changes in the mean metal-oxygen distance. However, their intensity is coupled to the degree of *d-p* mixing that accompanies octahedral site distortion. Tetrahedral coordination introduces considerable such mixing, resulting in a dramatic enhancement of the pre-edge features. In contrast, features on the main part of the edge can vary significantly in energy with more subtle changes in site geometry and are relatively sensitive to the mean metal-oxygen distance (Figure S6(c)). Fig. 3(b) presents the energies of all fitted pre-edge features in the studied sample. Gaussian deconvolution of the pre-edge region of the Ti-*K* XANES spectrum reveals two peaks in this region. Comparing pre-edge energies can be challenging. Similar to the Fe-*K* pre-edge, the 1 *s* to 3*d* transition is Laporte forbidden for a pure electric dipole interaction. However, it can be partially allowed by introducing a non-centrosymmetric orbital character into the excited state. This can be achieved through static or dynamic symmetry reduction or by electric quadrupole interactions. The absorption edge energies (conventionally defined as the energy at the first inflection point along the rising edge beyond the pre-edge region) were determined to be 4985 eV, corresponding to the Ti_0-4*p* state. This value is consistent with titanium in the +4-oxidation state. Due to insufficient data range, further investigation of the Ti coordination environment using EXAFS was not possible. Nevertheless, we can confidently conclude that the Ti in the sample measured in this study

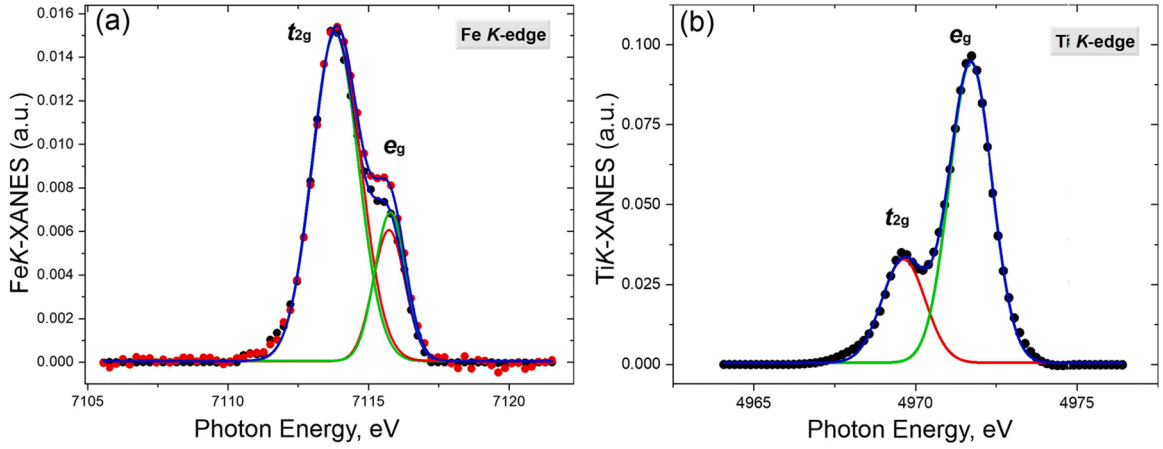

Fig. 3. Fe-*K* and Ti-*K* XANES spectra in the region of the pre-edge features showing Gaussian deconvolution. (a) – Fe-*K* XANES spectrum. (b) – Ti-*K* XANES spectrum. The symbols (circle) show the overall fit, which is composed of two Gaussian functions and a cubic spline background (already subtracted from the experimental spectrum).

primarily occupies octahedrally coordinated sites.

The Ti pre-*K*-edge, arising from the hybridization of 1 *s* with 3*d* transition orbitals, typically exhibits three main peaks due to the crystal field of the distorted octahedral coordination geometry. In the case of $FeTiO_3$ ilmenite, the hybridized 3*d* state with 4*p* and 4 *s* results in this distorted octahedral geometry [44]. This distortion causes the *d*-state to mix with a small 4*p* and 4 *s* character in the same energy distribution. The Ti pre-*K*-edge t_{2g} state peak is located at a lower energy than the e_g orbital state due to the ligand field of the TiF_6 octahedron [45]. According to Parlebas at al., the splitting of the t_{2g} state typically occurs due to the Jahn-Teller effect, resulting in three sub-non-degenerate peaks of the t_{2g} state attributable to the crystal field of the distorted TiF_6 octahedral configuration. In our study, we observe only two pre-edge peak regions of t_{2g} positioned at around 4965 – 4975 eV in the $FeTiF_6 \times 6\ H_2O$ sample. These peaks were obtained by background subtraction of pre-edge spectra from the edge energy baseline (Fig. S6 (b)) and deconvoluted for explicit peak composition (Fig. 3b). The first peak has been attributed to various origins, including quadrupolar 1 *s* to 3*d* (t_{2g}) transitions without dipole character and 3*d* (e_g) quadrupolar transitions [46,47]. However, it is predominantly characterized by the *K*-edge quadrupole t_{2g} transition character of the locally absorbed atom [35,45,48]. The high intensity and broadening in the second feature at 4971.7 eV can be attributed to Jahn-Teller distortion splitting corresponding to the Ti_0 $d(t_{2g})$-state with core-hold effect This region is mixed with the dipole-allowed Ti_0 4*p*-state [49,50].

It is noteworthy that the shape of the pre-edge Ti-*K* features at the absorption edge of titanium closely resembles that of minerals such as $FeTiO_3$ (ilmenite) and $CaTiSiO_5$ (titanite) [51]. For Fe-Ti oxides, a direct comparison was made between Ti *K*-edge XANES spectra for titanite and ilmenite, along with reference materials (TiO_2 and Ti_2O_3). The valence was estimated based on the shift in the position of the 1*s*-3*d* peak centroid energy. In our case, the centroid of the pre-edge Ti-*K* peak is 4970.67 eV, while for $FeTiO_3$ the centroid is 4970.9 eV and for $CaTiSiO_5$ - 4971.0 eV. By comparing these values with appropriate reference materials, we can infer that the coordination number of Ti^{3+} and Ti^{4+} in the sample in our study is six times higher. As illustrated in Fig. S6(b), the zero XMCD signal at the Ti-*K* pre-edge indicates the absence of 3*d*-4*p* mixed orbital polarization of the Ti atoms. Consequently, the Ti atoms do not possess any net magnetic moment. Therefore, the role of Ti in the magnetic interactions present in such materials is negligible.

4. Conclusion

Our combined DFT calculations and XANES/XMCD measurements provide a comprehensive understanding of the electronic structure, local distortions, and magnetic interactions in the $FeTiF_6 \times 6\ H_2O$ single crystal. Using DFT calculations, we investigated the electronic structure and local distortions of the 3*d* elements in the $FeTiF_6 \times 6\ H_2O$ single crystal. Our analysis revealed that the primary contribution to the local distortions in iron octahedra arises from the d^6 electron of iron 2+, leading to the dynamic Jahn-Teller effect and a reduction in energy. To further explore the electronic structure and magnetic interactions, as well as clarify the nature of magnetic transitions at low temperatures, we employed the XANES/XMCD techniques on the $FeTiF_6 \times 6\ H_2O$ single crystal. Analysis of the pre-edge XANES features of the Fe and Ti *K* absorption edges provided insights into the local environments and chemical states around the Ti and Fe atoms. The spectra exhibited electronic excitations in the pre-edge region and multiple scattering resonances at the side and top of the edge. Notably, the pre-edge features were found to be insensitive to the Ti-O bond length but sensitive to valence. Additionally, the pre-edge feature was observed to be sensitive to octahedral site distortion and the presence of octahedral Ti^{4+} due to the enhancement produced by *d-p* orbital mixing. The spectral features analysis suggests the presence of octahedral Ti^{4+} in the $FeTiF_6 \times 6\ H_2O$ single crystal. This observation is further corroborated by Mössbauer spectroscopy data, which confirmed the paramagnetic state of Fe^{2+} cations. In conclusion, our study demonstrates that iron sites in the Fe^{2+} oxidation state provide a unique paramagnetic contribution to the magnetization along the *b*-axis for the $FeTiF_6$ single crystal. Conversely, the absence of *3d* orbital polarization of the Ti atoms is evident from the zero XMCD signal at the Ti-*K* pre-edge, indicating that the Ti atoms do not possess a net magnetic moment. Consequently, the contribution of Ti to the magnetic interactions in such materials is considered negligible. Overall, the study provides insights into the electronic structure, local distortions, and magnetic interactions in the $FeTiF_6 \times 6\ H_2O$ single crystal, highlighting the role of iron in contributing to the paramagnetic behavior and the negligible contribution of titanium to the magnetic properties. Our findings contribute to a deeper understanding of the fundamental properties of $FeTiF_6 \times 6\ H_2O$ and provide valuable insights for the design and development of novel magnetic materials with tailored properties.

Funding

The reported study was funded by the Russian Science Foundation, Government of Krasnoyarsk Territory, and Krasnoyarsk Regional Foundation of Science under research project “Synthesis, spectral and magnetic properties of $ABF_6{\cdot}6\ H_2O$ systems, new materials for photonics.”, No. 23-22-10037 (https://rscf.ru/en/project/23–22-10037/). This work (research contribution of M.S.P.) was partially supported by

the Ministry of Science and Higher Education of the Russian Federation within the governmental assignment for Synchrotron radiation facility "SKIF", Boreskov Institute of Catalysis (project FWUR-2024-0040).

CRediT authorship contribution statement

Yulia Pyastolova: Methodology, Funding acquisition. **Michail Platunov:** Writing – review & editing, Writing – original draft, Visualization, Supervision, Project administration, Methodology, Investigation, Data curation, Conceptualization. **Natalia Fedorova:** Investigation. **Felix Tomilin:** Writing – review & editing, Visualization, Supervision, Methodology, Data curation. **Andrey Dubrovskiy:** Writing – review & editing, Visualization, Supervision, Project administration, Methodology, Investigation, Funding acquisition, Data curation, Conceptualization. **Natalia Laptash:** Methodology, Investigation. **Yuriy Knyazev:** Writing – review & editing, Visualization, Methodology, Investigation, Data curation, Conceptualization.

Declaration of Competing Interest

The authors declare that they have no known competing financial interests or personal relationships that could have appeared to influence the work reported in this paper.

Data availability

No data was used for the research described in the article.

Acknowledgements

The authors thank the Joint Supercomputer Center (JSCC) of the Russian Academy of Sciences. The authors would like to express their sincere gratitude to the ID12 beamline staff their exceptional dedication and professionalism in performing the synchrotron experiment during the challenging circumstances of the COVID-pandemic. We are particularly grateful to the postdocs, scientists, and technicians who took part in the experiment, ensuring its successful completion. We also gratefully acknowledge the provision of beamtime (Proposal HC-4375) by the European Synchrotron Radiation Facility (ESRF). The access to this world-class facility was instrumental in obtaining the high-quality data that formed the basis of our research. We are deeply appreciative of the contributions of all involved, and we extend our heartfelt thanks to each and every one of them.

Appendix A. Supporting information

Supplementary data associated with this article can be found in the online version at doi:10.1016/j.jallcom.2024.175104.

References

[1] T. Nakajima, H.B.T.-A.F.-B.M. for E.C. Groult (Eds.), Advanced Fluoride-Based Materials for Energy Conversion, Elsevier, 2015, https://doi.org/10.1016/C2013-0-18650-3.
[2] T. Nakajima, H.B.T.-F.M. for E.C. Groult (Eds.), Fluorinated Materials for Energy Conversion, Elsevier, Amsterdam, 2005, https://doi.org/10.1016/B978-0-08-044472-7.X5027-9.
[3] A. Tressaud, K.B.T.-P., E.P. of F.M. Poeppelmeier (Eds.), Photonic and Electronic Properties of Fluoride Materials, Elsevier, Boston, 2016, https://doi.org/10.1016/C2013-0-18987-8.
[4] A. Badawi, S.S. Alharthi, N.Y. Mostafa, M.G. Althobaiti, T. Altalhi, Effect of carbon quantum dots on the optical and electrical properties of polyvinylidene fluoride polymer for optoelectronic applications, Appl. Phys. A. 125 (2019) 858, https://doi.org/10.1007/s00339-019-3160-1.
[5] J.M. López-Encarnación, J.D. Burton, E.Y. Tsymbal, J.P. Velev, Organic multiferroic tunnel junctions with ferroelectric poly(vinylidene fluoride) barriers, Nano Lett. 11 (2011) 599–603, https://doi.org/10.1021/nl103650b.
[6] A.A. Udovenko, E.A. Goreshnik, E.B. Merkulov, N.M. Laptash, Mixed-valence hydrated iron fluoridotitanate: crystal structure and thermal behavior, J. Fluor. Chem. 249 (2021) 109853, https://doi.org/10.1016/j.jfluchem.2021.109853.
[7] S.K.D. Roy, B. Ghosh, Phase transition studies of paramagnetic crystals at low temperatures, Pramana 28 (1987) 573–581, https://doi.org/10.1007/BF03026694.
[8] L.C. Jackson, The magnetic susceptibility of ferrous fluosilicate at low temperatures, Philos. Mag. 4 (1959) 269–272, https://doi.org/10.1080/14786435908243263.
[9] A.A. Dubrovskiy, Y.V. Knyazev, D.A. Velikanov, A.M. Vorotynov, N.M. Laptash, Y. V. Gerasimova, Giant anisotropy of magnetic properties of hydrated iron fluoridotitanate single crystal, J. Alloy. Compd. 898 (2022) 162748, https://doi.org/10.1016/j.jallcom.2021.162748.
[10] T. Ohtsuka, Crystalline Field Splitting in Ferrous Fluosilicate, 1245–1245, J. Phys. Soc. Jpn. 14 (1959), https://doi.org/10.1143/JPSJ.14.1245.
[11] F. Varret, Pulsed magnetic field study of Fe2+ in some fluosilicates, J. Phys. Chem. Solids 37 (1976) 257–263, https://doi.org/10.1016/0022-3697(76)90085-8.
[12] F. Varret, Y. Allain, A. Miedan-Gros, Direct investigation of spin Hamiltonians DS2z by measuring magnetization during intense pulsed fields, Solid State Commun. 14 (1974) 17–20, https://doi.org/10.1016/0038-1098(74)90222-1.
[13] M. Karnezos, S.A. Friedberg, Magnetic and structural phase transitions in NiTiF6·6H2O, J. Appl. Phys. 49 (1978) 1380–1382, https://doi.org/10.1063/1.324998.
[14] A.A. Dubrovskiy, Y.V. Knyazev, Y.V. Gerasimova, A.A. Udovenko, N.M. Laptash, Influence of the Jahn-Teller effect on magnetic anisotropy in single crystals of fluorine hexahydrates of transition metals, Phys. Solid State 64 (2022) 1709, https://doi.org/10.21883/pss.2022.11.54194.406.
[15] J.S. Zhong, D.Q. Chen, X. Wang, L.F. Chen, H. Yu, Z.G. Ji, W.D. Xiang, Synthesis and optical performance of a new red-emitting ZnTiF6·6H2O:Mn4+ phosphor for warm white-light-emitting diodes, J. Alloy. Compd. 662 (2016) 232–239, https://doi.org/10.1016/j.jallcom.2015.12.075.
[16] T.P. Sinha, Influence of electron-phonon coupling on the Mössbauer quadrupole interaction in FeSiF6 · 6H2O, Phys. Status Solidi 169 (1992) 561–570, https://doi.org/10.1002/pssb.2221690227.
[17] Y.V. Gerasimova, A.S. Aleksandrovsky, N.M. Laptash, M.A. Gerasimov, A.S. Krylov, A.N. Vtyurin, A.A. Dubrovskiy, Spectroscopy of structurally disordered hydrated iron fluoridotitanate in the regions of vibrational and electronic excitations, Spectrochim. Acta Part A Mol. Biomol. Spectrosc. 264 (2022) 120244, https://doi.org/10.1016/j.saa.2021.120244.
[18] I.B. Bersuker, The jahn-teller effect in crystal chemistry and spectroscopy, Coord. Chem. Rev. 14 (1975) 357–412, https://doi.org/10.1016/S0010-8545(00)80266-0.
[19] G. Yu.V., K. A.S., V. A.N., L. N.M., P. E.I., D. A.A., G. M.A., Dynamic processes of the water sublattice in FeTiF6·xH2O·yD2O crystal, J. Raman Spectrosc. 53 (2022) 1704–1709. https://doi.org/10.1002/jrs.6430.
[20] K.V. Kamenev, S.K. Asadov, V.I. Kamenev, I.S. Maksimov, B.M. Todris, Phase transitions in the Mn-Zn fluorosilicate hexahydrates, J. Phys. Condens. Matter 13 (2001) 3709–3716, https://doi.org/10.1088/0953-8984/13/16/302.
[21] S.V. Mel'nikova, N.M. Laptash, M.V. Gorev, E.I. Pogoreltsev, Mixed-valence hydrated iron fluoridotitanate: synthesis, optics and calorimetry, J. Phys. Chem. Solids 142 (2020) 109444, https://doi.org/10.1016/j.jpcs.2020.109444.
[22] M. Bose, K. Roy, A. Ghoshray, ^{2}H NMR studies of structural phase transitions in some members of the deuterated ABF6, Phys. Rev. B. 35 (1987) 6619–6626, https://doi.org/10.1103/PhysRevB.35.6619.
[23] M. Tadic, D. Nikolic, M. Panjan, G.R. Blake, Magnetic properties of NiO (nickel oxide) nanoparticles: blocking temperature and Neel temperature, J. Alloy. Compd. 647 (2015) 1061–1068, https://doi.org/10.1016/j.jallcom.2015.06.027.
[24] J. Goulon, A. Rogalev, G. Goujon, C. Gauthier, E. Moguiline, A. Solé, S. Feite, F. Wilhelm, N. Jaouen, C. Goulon-Ginet, P. Dressler, P. Rohr, M.-O. Lampert, R. Henck, Advanced detection systems for X-ray fluorescence excitation spectroscopy, J. Synchrotron Radiat. 12 (2005) 57–69, https://doi.org/10.1107/S090904950402878X.
[25] C.A. Guido, E. Brémond, C. Adamo, P. Cortona, Communication: one third: a new recipe for the PBE0 paradigm, J. Chem. Phys. 138 (2013) 021104, https://doi.org/10.1063/1.4775591.
[26] A.D. Becke, Density-functional thermochemistry. III. The role of exact exchange, J. Chem. Phys. 98 (1993) 5648–5652, https://doi.org/10.1063/1.464913.
[27] D. Vilela Oliveira, J. Laun, M.F. Peintinger, T. Bredow, BSSE-correction scheme for consistent gaussian basis sets of double- and triple-zeta valence with polarization quality for solid-state calculations, J. Comput. Chem. 40 (2019) 2364–2376, https://doi.org/10.1002/jcc.26013.
[28] R. Dovesi, A. Erba, R. Orlando, C.M. Zicovich-Wilson, B. Civalleri, L. Maschio, M. Rérat, S. Casassa, J. Baima, S. Salustro, B. Kirtman, Quantum-mechanical condensed matter simulations with CRYSTAL, WIREs Comput. Mol. Sci. 8 (2018), https://doi.org/10.1002/wcms.1360.
[29] S.F. McWilliams, E. Brennan-Wydra, K.C. MacLeod, P.L. Holland, Density Functional Calculations for Prediction of 57 Fe Mössbauer Isomer Shifts and Quadrupole Splittings in β-Diketiminate Complexes, ACS Omega 2 (2017) 2594–2606, https://doi.org/10.1021/acsomega.7b00595.
[30] P. Blaha, P. Dufek, K. Schwarz, H. Haas, Calculation of electric hyperfine interaction parameters in solids, Hyperfine Inter. 97–98 (1996) 1–10, https://doi.org/10.1007/BF02150164.
[31] R. Sternheimer, On nuclear quadrupole moments, Phys. Rev. 80 (1950) 102–103, https://doi.org/10.1103/PhysRev.80.102.2.
[32] R. Sternheimer, On nuclear quadrupole moments, Phys. Rev. 84 (1951) 244–253, https://doi.org/10.1103/PhysRev.84.244.
[33] S. Lauer, V.R. Marathe, A. Trautwein, Sternheimer shielding using various approximations, Phys. Rev. A. 19 (1979) 1852–1861, https://doi.org/10.1103/PhysRevA.19.1852.

[34] Z.Y. Wu, G. Ouvrard, P. Gressier, C.R. Natoli, Ti and O K edges for titanium oxides by multiple scattering calculations: comparison to XAS and EELS spectra, Phys. Rev. B. 55 (1997) 10382–10391, https://doi.org/10.1103/PhysRevB.55.10382.
[35] D. Cabaret, A. Bordage, A. Juhin, M. Arfaoui, E. Gaudry, First-principles calculations of X-ray absorption spectra at the K-edge of 3d transition metals: an electronic structure analysis of the pre-edge, Phys. Chem. Chem. Phys. 12 (2010) 5619, https://doi.org/10.1039/b926499j.
[36] E. Cottrell, K.A. Kelley, The oxidation state of Fe in MORB glasses and the oxygen fugacity of the upper mantle, Earth Planet. Sci. Lett. 305 (2011) 270–282, https://doi.org/10.1016/j.epsl.2011.03.014.
[37] L. Galoisy, G. Calas, M.-A. Arrio, High-resolution XANES spectra of iron in minerals and glasses: structural information from the pre-edge region, Chem. Geol. 174 (2001) 307–319, https://doi.org/10.1016/S0009-2541(00)00322-3.
[38] P. Glatzel, A. Mirone, S.G. Eeckhout, M. Sikora, G. Giuli, Orbital hybridization and spin polarization in the resonant 1s photoexcitations of α-Fe2O3, Phys. Rev. B. 77 (2008) 115133, https://doi.org/10.1103/PhysRevB.77.115133.
[39] A.J. Berry, H.S.C. O'Neill, K.D. Jayasuriya, S.J. Campbell, G.J. Foran, XANES calibrations for the oxidation state of iron in a silicate glass, Am. Mineral. 88 (2003) 967–977, https://doi.org/10.2138/am-2003-0704.
[40] L.A. Grunes, Study of the K edges of 3d transition metals in pure and oxide form by x-ray-absorption spectroscopy, Phys. Rev. B. 27 (1983) 2111–2131, https://doi.org/10.1103/PhysRevB.27.2111.
[41] G.A. Waychunas, Synchrotron radiation XANES spectroscopy of Ti in minerals: effects of Ti bonding distances, TI Valence, and Site Geometry on Absorption Edge Structure, Am. Mineralogist; (USA), 72:1-2; ISSN 0003-004X.
[42] F. Farges, G.E. Brown, J.J. Rehr, Coordination chemistry of Ti(IV) in silicate glasses and melts: I. XAFS study of titanium coordination in oxide model compounds, Geochim. Cosmochim. Acta 60 (1996) 3023–3038, https://doi.org/10.1016/0016-7037(96)00144-5.
[43] M.R. Ackerson, N.D. Tailby, E.B. Watson, XAFS spectroscopic study of Ti coordination in garnet, Am. Mineral. 102 (2017) 173–183, https://doi.org/10.2138/am-2017-5633.
[44] W. Phoohinkong, K. Boonyarattanakalin, W. Mekprasart, S. Pavasupree, W. Pecharapa, Nonlocal XANES pre-edge feature of FeTiO3 ilmenite-type at Ti and Fe K-edge, Radiat. Phys. Chem. 174 (2020) 108919, https://doi.org/10.1016/j.radphyschem.2020.108919.
[45] J.C. Parlebas, M.A. Khan, T. Uozumi, K. Okada, A. Kotani, Theory of many-body effects in valence, core-level and isochromat spectroscopies along the 3d transition metal series of oxides, J. Electron. Spectrosc. Relat. Phenom. 71 (1995) 117–139, https://doi.org/10.1016/0368-2048(94)02262-3.
[46] N. Jiang, D. Su, J.C.H. Spence, Determination of Ti coordination from pre-edge peaks in Ti K-edge XANES, Phys. Rev. B. 76 (2007) 214117, https://doi.org/10.1103/PhysRevB.76.214117.
[47] C. Yogi, K. Kojima, T. Hashishin, N. Wada, Y. Inada, E. Della Gaspera, M. Bersani, A. Martucci, L. Liu, T. Sham, Size Effect of Au nanoparticles on TiO2 crystalline phase of nanocomposite thin films and their photocatalytic properties, J. Phys. Chem. C 115 (2011), https://doi.org/10.1021/jp110581j.
[48] Y. Joly, D. Cabaret, H. Renevier, C.R. Natoli, Electron population analysis by full-potential X-ray absorption simulations, Phys. Rev. Lett. 82 (1999) 2398–2401, https://doi.org/10.1103/PhysRevLett.82.2398.
[49] J.W.J. Slavin, U. Jarori, D. Zemlyanov, A. Ivanisevic, Characterization of amino acid adlayers on InAs surfaces using X-ray photoelectron spectroscopy, J. Electron. Spectrosc. Relat. Phenom. 172 (2009) 47–53, https://doi.org/10.1016/j.elspec.2009.03.006.
[50] R.A.P. Ribeiro, S.R. de Lázaro, Structural, electronic and elastic properties of FeBO3 (B = Ti, Sn, Si, Zr) ilmenite: a density functional theory study, RSC Adv. 4 (2014) 59839–59846, https://doi.org/10.1039/C4RA11320A.
[51] F. Leitzke, R. Fonseca, J. Goettlicher, R. Steininger, S. Jahn, C. Prescher, M. Lagos, Ti K-edge XANES study on the coordination number and oxidation state of Titanium in pyroxene, olivine, armalcolite, ilmenite, and silicate glass during mare basalt petrogenesis, Contrib. Mineral. Petrol. 173 (2018), https://doi.org/10.1007/s00410-018-1533-7.